

Article

# Effect of Direct Energy Deposition Process Parameters on Single-Track Deposits of Alloy 718

Suhas Sreekanth <sup>1,\*</sup>, Ehsan Ghassemali <sup>2</sup>, Kjell Hurtig <sup>1</sup>, Shrikant Joshi <sup>1</sup> and Joel Andersson <sup>1</sup>

<sup>1</sup> Department of Engineering Science, University West, 46186 Trollhättan, Sweden; kjell.hurtig@hv.se (K.H.); shrikant.joshi@hv.se (S.J.); joel.andersson@hv.se (J.A.)

<sup>2</sup> Department of Materials and Manufacturing, Jönköping University, 55111 Jönköping, Sweden; Ehsan.Ghassemali@ju.se

\* Correspondence: suhas.sreekanth@hv.se; Tel.: +46-520-223-484

Received: 5 December 2019; Accepted: 5 January 2020; Published: 7 January 2020



**Abstract:** The effect of three important process parameters, namely laser power, scanning speed and laser stand-off distance on the deposit geometry, microstructure and segregation characteristics in direct energy deposited alloy 718 specimens has been studied. Laser power and laser stand-off distance were found to notably affect the width and depth of the deposit, while the scanning speed influenced the deposit height. An increase in specific energy conditions (between 0.5 J/mm<sup>2</sup> and 1.0 J/mm<sup>2</sup>) increased the total area of deposit yielding varied grain morphologies and precipitation behaviors which were comprehensively analyzed. A deposit comprising three distinct zones, namely the top, middle and bottom regions, categorized based on the distinct microstructural features formed on account of variation in local solidification conditions. Nb-rich eutectics preferentially segregated in the top region of the deposit (5.4–9.6% area fraction,  $A_f$ ) which predominantly consisted of an equiaxed grain structure, as compared to the middle (1.5–5.7%  $A_f$ ) and the bottom regions (2.6–4.5%  $A_f$ ), where columnar dendritic morphology was observed. High scan speed was more effective in reducing the area fraction of Nb-rich phases in the top and middle regions of the deposit. The  $\langle 100 \rangle$  crystallographic direction was observed to be the preferred growth direction of columnar grains while equiaxed grains had a random orientation.

**Keywords:** laser metal deposition (LMD); columnar dendritic morphology; constitutional supercooling; columnar to equiaxed transition (CET); high deposition rate

## 1. Introduction

Directed Energy Deposition (DED) is an additive manufacturing (AM) process utilized for varied applications such as rapid prototyping, cladding, building components and part features, in-situ alloying, repair and refurbishing applications [1–3]. The process offers advantages such as: (a) the capability to achieve high deposition volumes in a large build envelope [4]; (b) the ability to deposit compositionally and/or functionally graded materials [5–7]; (c) ability to deposit materials on top of flat and curved substrate surface; and (d) adaptability to existing CNCs and robotic systems, which provides an edge over metal powder-bed fusion (PBF) processes. The above benefits offset the relative inadequacy of the process to produce near-net-shape part features of geometrical complexity that can be accomplished through PBF processes.

In the present manuscript, DED refers to a variant having laser as the energy source which uses powder form of Alloy 718 as feedstock. Also, high deposition rate -directed energy deposition (HDR-DED) process is of specific interest in this work as it can have direct implications on processing times and economics. Most of the work conducted thus far has involved feed rates lower than 0.5 kg/h,

termed as 'low deposition rates' (LDR) [8,9]. This shift from LDR to HDR is expected to influence various properties of deposits such as grain structure, morphology, defect content and geometrical characteristics. These characteristics of the HDR-DED process was studied by Zhong et al. [10] in terms of track porosity, wettability, deposit height and width with varied process parameters such as power, feed rate and scanning speeds. Porosity decreased with increased laser power whereas width of the deposit increased with increased power or decreased feed rate. Both height and width of the tracks decreased with increased scanning speed. Although anisotropic properties, porosity content and elemental segregation properties were reported by Zhong et al. [11] for HDR-DED samples, the tensile properties after Hot Isostatic Pressing (HIP) + heat treatment was comparable to wrought Alloy 718. A brief account of microstructure and its mechanical properties were reported for HDR-DED of Alloy 718 [12], but a more detailed analysis of single-track deposit is necessary for an improved process understanding that can be subsequently utilized for 3D-deposition of HDR builds. In the LDR-DED process, it is often reported that increased feed produces increased height and decreased depth of the deposit, but the effect on width is minimal.

Many studies have considered Alloy 718 as the deposition material in the DED process owing to a combination of factors, including the alloy's widespread usage particularly in the aerospace industry and the attractive nature of the DED process as a cladding and repair technique. Alloy 718 is used in the hot section region of gas turbine applications up to a temperature of 650 °C [13–15]; however, it is vulnerable to Nb-segregation, an element which influences the precipitation of strengthening phases as often reported by numerous researchers [16–19]. Various strategies have been employed in controlling and minimizing these Nb-rich eutectics in both welding [20–22] and AM practices. Xiao et al. [23,24] accommodated a strategy that involved variation of laser modes between continuous-wave (CW) and quasi-continuous wave (QCW), wherein the cooling rates achieved by QCW mode were an order of magnitude higher compared to CW mode. An equiaxed dendritic microstructure was obtained in QCW mode as opposed to CW mode which produced columnar dendritic microstructures. Chen et al. [25] studied the formation and segregation of laves phase by manipulation of laser energy distribution in the form of flat-top and Gaussian beams. Gaussian beam distribution yielded higher fraction of laves phase that increased along the build height (6–11% volume fraction) as opposed to flat-top distribution (5–6% volume fraction) throughout the deposit. However, the cooling rates for Gaussian beams predicted from dendrite arm spacing were five times higher compared to flat-top beam. This resulted in an increased size of precipitates and consequently increased tensile strength in case of the flat-top beam condition.

A thermal model that predicted the cooling rate at varied powers and scanning speeds was developed by Amine et al. [26] for different scanning strategies. Low power and high scanning speed conditions yielded higher cooling rates. Numerical modeling work by Nie et al. [27] investigated the formation of microstructure in Alloy 718 by prediction of cooling rates along the deposit height for varied powder sizes and thence the secondary dendritic arm spacing along the deposit centerline. Further, the concentration of the laves phase was predicted based on the variations in temperature gradient and cooling rates [28]. A low temperature gradient and high cooling rate was predicted to be necessary for formation of a discrete laves phase instead of precipitation of continuous bands along inter-dendritic regions. The effect of process parameters and scanning strategies were experimentally studied by Parimi et al. [29] and the study concluded that grain morphology can alter Nb-rich segregation. A similar work was reported by Dinda et al. [30] wherein different scanning strategies were employed to control the texture of DED deposited Alloy 718. Most of the modelling and microstructural work discussed above pertains to LDR-DED process.

Generally, the multiple tracks in DED have been distinguished into top, middle and bottom regions based on phase fraction analysis and segregation characteristics have been studied along the build height [25,31,32]. As a precursor to developing a robust HDR-DED process, it is desirable to understand the impact of process parameters on the characteristics of these top, middle and bottom regions of a single track deposit. The present work primarily concerns identification and control of such

microstructural and segregation patterns in discrete regions of single-track deposits of Alloy 718. The control of segregation is particularly important in DED repair and building part features applications as they are often introduced to direct aging heat treatment after deposition. Variations in phase fraction of segregation can cause heterogeneities in the deposit, rendering ineffective precipitation strengthening in local areas of segregation, which could prove detrimental to material properties. Strategies to control and nullify such compositional and phase heterogeneities by suitable manipulation of process parameters is an intended outcome of this study. Also, the effect of process parameters on microstructure and texture development is considered for single-track deposits.

## 2. Materials and Methods

The deposited samples were built on an ISEL M40 4-Axis CNC machine bed with COAX-50 (Fraunhofer ILT, Aachen, Germany), otherwise referred to as D50-coaxial nozzle. An IPG YLR-6000S, a 6 kW Ytterbium (Yb) doped fiber laser (IPG Photonics, Burbach, Germany) was used as the laser source coupled with a Permana Collimator of 200 mm focal length (Permana Lasersystems AB, Mölndal, Sweden) with Optoskand fiber of 800  $\mu\text{m}$  diameter (Optoskand AB, Mölndal, Sweden). The powder feed-rate was controlled through a dual D2-volumetric powder-feeder arrangement from Uniqucoat Technologies (Uniqucoat Technologies LLC, Oilville, VA, United States). Argon was used as both the carrier gas and shielding gas throughout the deposition process.

Gas Atomized (GA) Alloy 718 powder with a particle size range of 40–105  $\mu\text{m}$  (D10, D50 and D90 of 47  $\mu\text{m}$ , 65  $\mu\text{m}$  and 83  $\mu\text{m}$  respectively) was used as feedstock. Table 1 presents the nominal compositions of the powder and the substrate complying to the standard F3055-14a [33] and ASTM B670-07 [34] respectively.

**Table 1.** Chemical composition (wt.%) of Alloy 718 powder and substrate.

Elements	Ni	Cr	Fe	Nb + Ta	Mo	C	Ti	Al
<b>Powder</b>	52.89	18.7	18.52	4.9	2.94	0.05	0.92	0.61
<b>Substrate</b>	53.57	18.7	17.58	4.97	2.89	0.04	0.91	0.59
Elements	Co	Ta	B	Cu	Mn	Si	P	S
<b>Powder</b>	0.11	<0.01	<0.001	<0.1	0.05	0.19	0.005	0.004
<b>Substrate</b>	0.25	0.004	0.002	0.23	0.09	0.06	0.008	0.001

Single tracks were deposited on wrought Alloy 718 substrate with dimensions 150 mm  $\times$  60 mm  $\times$  3.2 mm. Two tracks of length 55 mm were deposited for each parametric set to check for repeatability. A reduced multi-level factorial design was considered in the present study with three variable factors: power (P), scanning speed (V) and laser stand-off distance ( $L_o$ ). P was varied at three levels: 1200, 1600, 2000 W; V was varied at two levels: 900, 1100 mm/min; and  $L_o$  was varied at two levels: 9.5, 13 mm. Another parameter set (P = 1800 W; V = 1100 mm/min;  $L_o$  = 13 mm) close to high power condition with was considered for verification of results. Other parameters such as powder feed rate ( $M_p$ ): 1.2 kg/hr, carrier gas flow ( $G_c$ ): 5 L/min and shielding gas flow rate ( $G_s$ ): 12 L/min were kept constant. The effect of V was studied at intermediate power of 1600 W alone reducing the iterations in design. The resulting nine parametric sets, as shown in Table 2, were analyzed to study the effect of P, V and  $L_o$  parameters on various deposit characteristics such as deposit geometry, microstructural morphology and segregation of niobium-rich (Nb-rich) eutectic phases.  $L_o$  of 9.5 mm and 13 mm above the substrate in the divergence part of laser beam corresponded to a laser spot diameter ( $D_s$ ) of 1.8 mm and 2.3 mm, respectively.

The sample preparation for metallographic investigations involved a series of grinding and polishing steps performed on a Buehler Eco-Met 300 machine (ITW Test and Measurement GmbH, Esslingen, Germany) followed by electrolytic etching with oxalic acid to reveal the presence of Nb-rich eutectic phases that were predicted to form during solidification of Alloy 718. Optical microscopy was

carried out with the aid of a Zeiss Axioscope 5 coupled with AxioCam 506 (Carl Zeiss AB, Stockholm, Sweden). For higher magnifications needed for phase fraction analyses and phase identification, a Hitachi TM3000 table-top SEM (Hitachi High-Technologies Europe GmbH, Stockholm, Sweden), coupled with a Bruker Scan Generator and an Oxford Instruments X-Max 20 Electron Diffraction Spectroscopy (EDS) detector (Oxford Instruments NanoAnalysis, Stockholm, Sweden) were utilized. Electron Backscatter Diffraction (EBSD) analysis was performed with JEOL7001F SEM/EDAX-Hikari (super) detector (JEOL Nordic AB, Sollentuna, Sweden) combination. TEAM 4.5 and OIM (TSL) version 8 (Ametek GmbH, Weiterstadt, Germany) were used for data acquisition and analyses.

**Table 2.** Parameter sets used in the designed experiments.

Laser Power, P (W)	Scanning Speed, V (mm/min)	Laser Stand-Off Distance, $L_o$ (mm)	Designation
1200	1100	9.5	1
1600	900	9.5	2
2000	1100	9.5	3
1200	1100	13	4
1600	900	13	5
2000	1100	13	6
1800	1100	13	7
1600	1100	9.5	8
1600	1100	13	9

A Gaussian power distribution was obtained for the parametric conditions considered (Figure 1a). A typical beam profile and power distribution is shown in Figure 1 for  $P = 1200$  W and  $L_o = 9.5$  mm. The power intensity at  $L_o = 9.5$  mm was higher compared to  $L_o = 13$  mm for all laser powers (1200, 1600 and 2000 W) as recorded in Table 3.

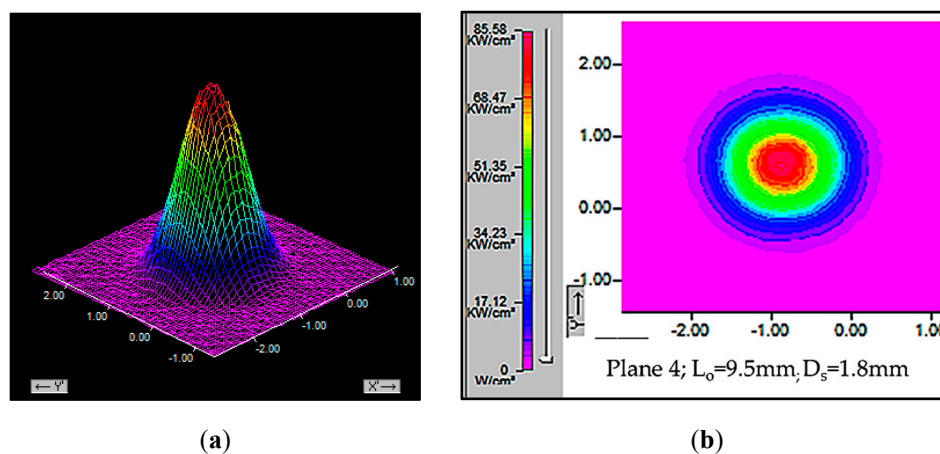


**Figure 1.** (a) Gaussian distribution of power intensity; (b) laser beam profile for  $P$  of 1200 W and  $L_o$  of 9.5 mm above the focal point.

**Table 3.** Peak power intensity for different  $L_o$  at varying  $P$ .

Laser Power $P$ in W	Peak Power Intensity	
	$L_o = 9.5$ mm	$L_o = 13$ mm
	Peak Power, kW/cm <sup>2</sup>	Peak Power, kW/cm <sup>2</sup>
1200	85.6	52.6
1600	114	70
2000	142.5	87.7

A typical cross-section of a single-track DED deposit depicting geometric measurements of interest is illustrated in Figure 2. The DED material showed a distinct appearance compared to the wrought microstructure present in the substrate region. The horizontal dotted line marked in the figure is indicative of the original substrate surface before deposition. The values of height (H), width (W) and depth (D) were obtained by measuring dimensions as in Figure 2. The measurement of area of deposition and dilution was done using Image-J software (version 1.5). The area above the fine dotted line indicated the area of deposit ( $A_d$ ) and the area below indicated area of dilution ( $A_s$ ), measured in  $\text{mm}^2$ . Dilution percentage was obtained by the equation;

$$\% \text{Dilution} = \frac{A_s}{A_s + A_d} \quad (1)$$

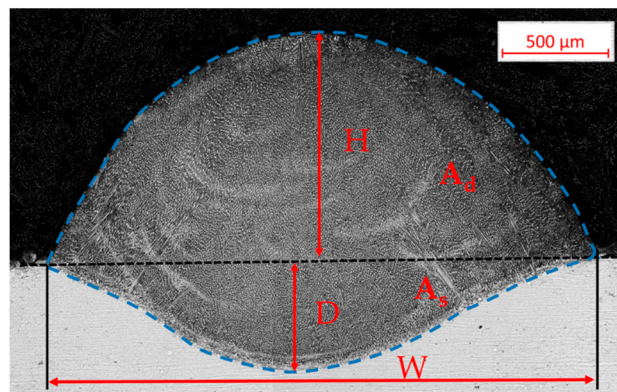


**Figure 2.** A typical directed energy deposition (DED) deposit depicting geometric measurements of interest.

The powder capture efficiency ( $\eta$ ) can provide useful insights into the different geometrical aspects of deposits, which can be calculated by the equation [10];

$$\eta = \frac{\rho \times V \times A_d}{M_p} \quad (2)$$

where  $\rho$  represents the density of Alloy 718.

As  $M_p$  in the present set of experiments was kept constant, a specific energy term (measured in  $\text{J}/\text{mm}^2$ ) can be determined by the following relationship between process parameters [31];

$$\text{Specific Energy} = \frac{P}{V \times D_s} \quad (3)$$

Quantification of Nb-rich phases was performed using Image-J software. The threshold value for brightness/contrast ratios were assigned based on the SEM images. Further, a binary mask was applied for quantification of results.

The determination of non-equiaxed grain-size was performed as per the ASTM E112-13 standard [35]. The mean length of intercept ( $\bar{l}$ ) was calculated in three co-ordinate axes along the geometry of the deposit to measure the average grain size. ASTM number (G) was calculated by using the relation;

$$G = (-6.644 \log_{10} \bar{l}) - 3.288 \quad (4)$$

### 3. Results and Discussions

All the parameter sets considered in this experimental design (see Table 2) yielded sound and continuous deposition of material. In the following section geometrical characteristics, morphological characteristics and segregation observed at varied processing conditions are reported and discussed.

### 3.1. Deposit Geometry

A desirable attribute of AM is to minimize material removal through machining processes and hence calls for accurate deposit geometries, attainable by controlling process parameters. Geometric measurements were compiled by averaging six different sections. The values of  $H$  varied between 900  $\mu\text{m}$  and 1300  $\mu\text{m}$ ,  $W$  varied between 1900  $\mu\text{m}$  and 2600  $\mu\text{m}$  and  $D$  varied between 120  $\mu\text{m}$  and 720  $\mu\text{m}$ . It can be noted from Figure 3a, that the total area ( $A_s + A_d$ ) and  $A_d$  increased with increase in specific energy. Figure 3b shows the variation in  $\eta$  at  $L_o = 9.5$  mm and 13 mm. It shows an increasing trend with a product of specific energy and laser spot diameter. As the stand-off distance increased, the area of heat input increased due to larger spot diameter, thereby melting more powder.

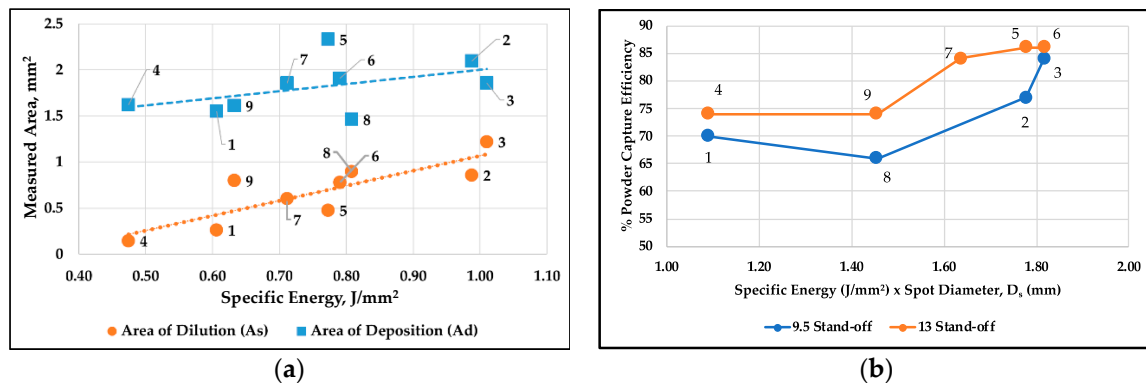


**Figure 3.** (a) Plot of energy input vs. area of deposit ( $A_d$ ) and area of dilution ( $A_s$ ); (b) plot of % powder capture efficiency vs specific energy  $\times$  laser spot diameter. Note: numbers adjacent to data-points in (a,b) correspond to parameter set numbers summarized in Table 2.

Energy from the laser source is primarily utilized for melting the feedstock powder continuously fed into a melt-pool in a DED process. However, a part of the energy is also utilized for melting the substrate to create the melt-pool which determines the amount of dilution. When the feed rate is low, a higher amount of energy is available for melting the substrate yielding high dilutions, given other parametric conditions remain the same [36]. The values of dilution measured are depicted in Figure 3a for various process parameters and found to vary between 9% and 39%.

#### 3.1.1. Effect of Laser Power and Laser Stand-Off Distance on the Geometry of Deposits

Three different laser powers: 1200, 1600 and 2000 W were employed at two different laser stand-off distances of 9.5 mm and 13 mm. An additional parameter of  $P = 1800$  W with  $L_o = 13$  mm was also considered as shown in parameter set 7. Figure 4 shows the effect of  $P$  on  $H$ ,  $W$  and  $D$  of deposits having processing conditions as tabulated in Table 2.

$H$  decreased when  $P$  increased from 1200 W to 1600 W and increased when  $P$  was further increased to 2000 W.  $\eta$  depicted in Figure 3c were 66% and 72% for  $L_o$  of 9.5 mm and 13 mm respectively at  $P$  of 1600 W (decreased  $H$  conditions), which is quite low, hence the decrease in  $H$  measured. Decreased  $\eta$  decreased  $M_p$ , which in turn decreased the value of  $H$ ; as  $H$  is a variable dependent on  $M_p$ . Similar results were obtained by Chen et al. [31], wherein the effect of  $P$  on  $H$  was not ascertained. A study by Segerstark et al. [32] concluded that decrease in  $V$  and increase in  $M_p$  increased  $H$ , but  $P$  was found to have negligible effect on  $H$ . A study by Corbin et al. [37] showed that  $H$  remained fairly constant over a certain  $P$  (250–400 W) and gradually increased with further increase in  $P$  when other process parameters remained unchanged, which ascertains the result obtained in the present study. Change in  $L_o$  did not show any significant effect on  $H$  as seen in Figure 4a.

$W$  increased with  $P$  in both cases of  $L_o$  as shown in Figure 4b. A relatively large amount of energy was available at 2000 W compared to 1200 W and 1600 W, increasing the shape and size of the melt-pool resulting in increased  $W$ . The power distribution in case of  $L_o = 13$  mm acts upon a larger area due to

$D_s$  (2.3 mm) compared to  $L_o = 9.5$  mm ( $D_s = 1.8$  mm) and thereby increases  $W$ . The powder capture efficiency has minimal effects on  $W$ , and same is seen in case of  $P = 1600$  W as  $D_s$  was the dominant factor. As reported in the introduction, decreased  $M_p$  leads to increased  $W$ , as more lateral heat transfer takes place for melting the substrate and providing a larger area for the melt flow.

Figure 4c indicates that  $L_o$  of 9.5 mm had higher  $D$  compared to the  $L_o$  of 13 mm due to higher energy density at 9.5 mm (Table 3) which melted more material. The specific energy had a noticeable effect on  $D$ , as deposits 2 and 3 indicated higher dilution and in the other extreme, deposits 1 and 4 showed lower levels of dilution (Figure 3a).

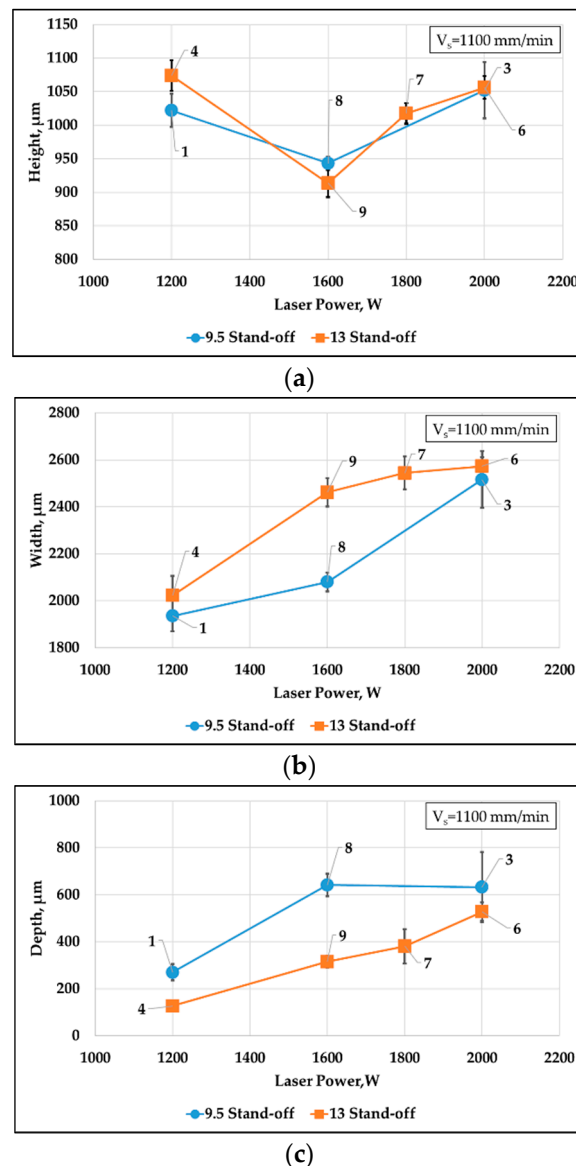


**Figure 4.** Influence of laser power of 1200, 1600, 1800 and 2000 W on (a) height; (b) width; and (c) depth of deposits at laser stand-off distances of 9.5 mm and 13 mm at a constant scanning speed of 1100 mm/min.

### 3.1.2. Effect of Scanning Speed and Laser Stand-Off Distance on the Geometry of Deposits

For studying the effects of scanning speed and laser stand-off distance on geometry, single-tracks processed at two different  $V$  of 900 mm/min and 1100 mm/min with  $L_o$  of 9.5 mm and 13 mm at  $P$  of 1600 W were considered, as in parameter sets 2, 5, 8 and 9.

It can be seen in Figure 5a that the  $H$  was insensitive to the changes in  $L_o$ . However, with increased  $V$ ,  $H$  decreased.  $W$  showed a similar trend as  $H$  with respect to  $V$ . An increased  $V$  showed a decline in

W, although the decline was less significant as compared to H. The effect of  $L_o$  on W was significant as seen in Figure 5b. A lower  $L_o$  of 9.5 mm yielded lower W compared to  $L_o$  of 13 mm. D showed a varied relationship as compared to H and W depicted in Figure 5c.

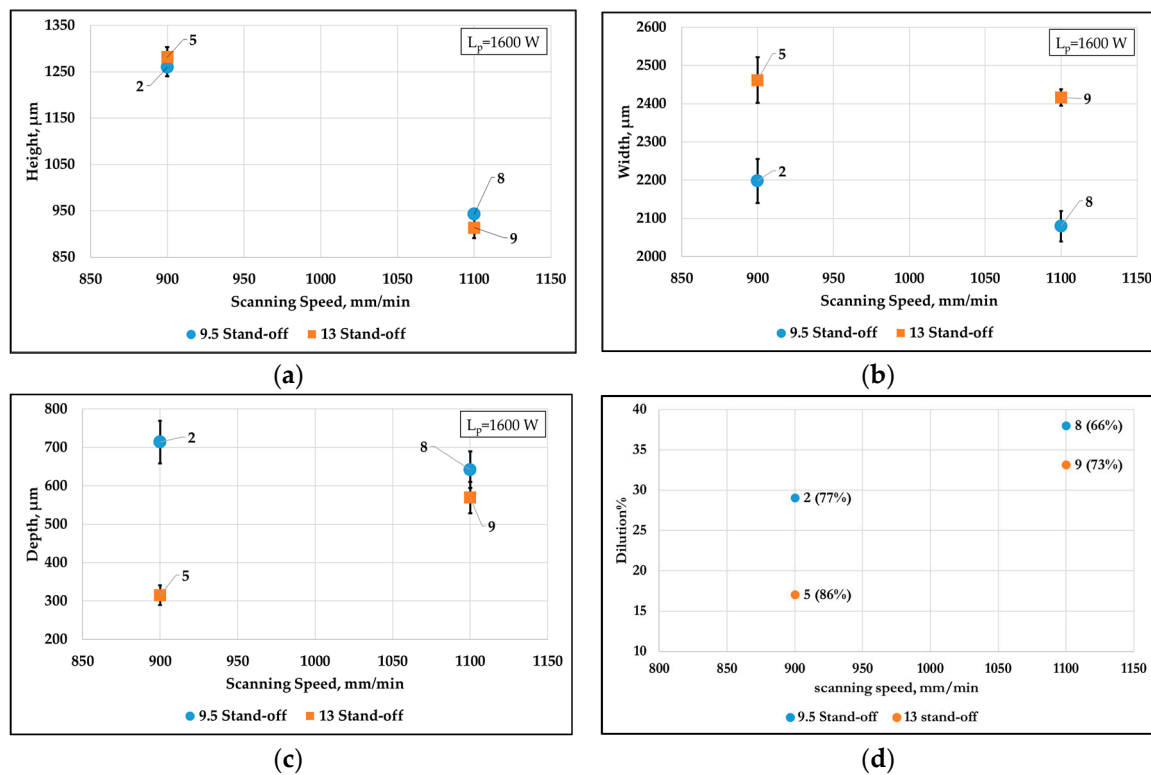


**Figure 5.** Influence of scanning speeds of 900 mm/min and 1100 mm/min on (a) height, (b) width, (c) depth, (d) %dilution of deposits at laser stand-off distances of 9.5 mm and 13 mm at a constant laser power of 1600 W.

With increased  $V$ , the specific energy decreased due to decrease in interaction time of laser beam on substrate. This reduced the amount of material melted per unit time resulting in decreased  $H$  and  $W$ , thereby lowering powder capture efficiency (within parentheses) as shown in Figure 5d. The change in  $W$  can be explained by increased  $D_s$  associated with increased  $L_o$ . The energy for substrate melting increased with increased  $V$  as the  $M_p$  was constant, and the amount of powder available for melting depleted with increased  $V$  (defined as line mass,  $M_p/V$ ).

### 3.2. Grain Morphology

The cross-sectional morphology for one-half of a single-track deposit is shown in Figure 6a, as the other half of the cross-section was symmetrical. The deposit can be broadly distinguished into three separate regions, the top, the middle and the bottom areas based on morphological differences observed in microstructural features present in these discrete regions depicted by Figure 6b–d respectively.

The bottom and middle regions closer to the substrate can dissipate heat much faster compared to the top region, and hence yielded columnar dendritic microstructures and relatively lower segregation of Nb-rich phases [38]. An interplay between thermal gradient ( $G$ ) and growth rate ( $R$ ) determined the cooling rate and substructure formation during solid-liquid (S/L) transformation. The  $G$  is higher in the bottom region where relatively cooler substrate was in contact with the melt-pool which led to a high  $G/R$  ratio which preferentially formed columnar dendritic structures as the planar and cellular growth fronts terminated prematurely [39,40]. The  $G$  value gradually decreased towards the top region of the deposit where equiaxed grain morphology was noticed [38,40]. The dendritic growth at the top edge of the deposit indicated a secondary growth front that nucleated from partially melted powders

and also due to shielding gas interaction with the melt-pool, that provided a suitable condition for heterogeneous nucleation away from the solidification front [32]. The heat dissipation by partially melted powder particles is minimal as compared to the substrate, and the cooling rates achieved in this region are low compared to the bottom of the deposit.

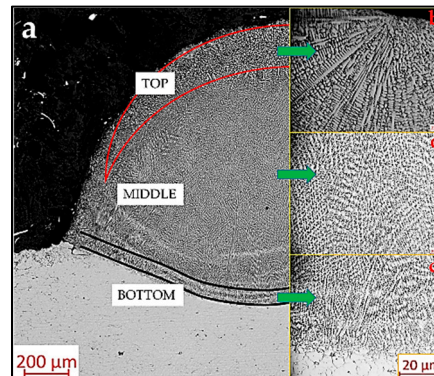


**Figure 6.** (a) A typical morphology of a deposit; magnified images of (b) top; (c) middle; (d) bottom regions of the bead.

‘Fan-like’ microstructures similar to those observed in the top region of the deposit were reported by Antonsson et al. [41], that narrated the effect of cooling rates and solidification structures formed of Alloy 718 by Levitation Casting (LC) technique having an undercooling of 40 °C at the highest growth temperature of 1300 °C, leading to an estimated cooling rate of 15,000 °C/s. Dendrites formed in the top region of DED deposits considered in this study are well-developed compared to the LC technique, indicating lower undercooling and relatively low cooling rates of 100–600 °C/s [27,42].

### 3.2.1. EBSD Mapping

The inverse pole figure (IPF) maps and respective (001) pole figures depicting the growth orientation and textures formed in different region of deposits 1, 2, 3, 8 and 9 are as shown in Figure 7. Columnar grains were observed in the middle and bottom regions of the deposit for all five conditions considered. The grains at the bottom that grew epitaxially from the substrate were comparatively smaller compared to those found in the middle region of the deposit [43,44]. Cooling rates ( $\epsilon$ ) are considered critical in influencing the microstructural scales formed during solidification [38]. The cooling rate decreases gradually with the height of the deposit, thereby producing relatively larger columnar structures away from the substrate.

Another commonality in most deposits analyzed was the orientation of grains. Apart from deposit 1, most grains were oriented in  $\langle 110 \rangle$  and  $\langle 111 \rangle$  directions for samples 2, 3, 8 and 9. The IPFs in Figure 7 showed moderate textures (3.5 to 5.6) along  $\langle 110 \rangle$  directions in (001) pole figures. The orientation of the grains was influenced primarily by the direction of heat flow under high cooling rate conditions. Maximum heat-flux occurs in the direction perpendicular to the S/L growth front. The S/L growth front represented the fusion line between the melt-pool and the substrate at the start of solidification [40]. Hence, a columnar grain evolved from the interaction surface at the substrate in the opposite direction to the heat flux. Further, since the melt-pool shape was dynamic and curved at the fusion-line between the substrate and melt-pool, the values of  $G$  and  $R$  constantly changed. This influenced the growth direction of columnar grains that originated from the fusion-line to the deposit center-line [38]. Deposits of 2, 3, 8 and 9 conditions had high dilutions as opposed to the deposit 1, which showed the lowest dilution and depicted the strongest texture of the five conditions considered (at 7.8) in the  $\langle 100 \rangle$  direction, the preferred growth direction in the case of cubic crystals. The interaction angle ( $\alpha$ ) which was the angle between the substrate surface before deposition and a tangent to fusion line at the deposit edge (Figure 7a), changed with the dilution and is equal to 20° for deposit 1 which was considerably smaller compared to deposits 2, 3, 8 and 9 (43°, 46°, 51°, 45° respectively). The tendency of grain

growth towards the weld centerline was affected by the amount of dilution indicated by  $\alpha$ . The grains oriented in  $\langle 110 \rangle$  were observed to originate from the fusion line with  $\alpha$  nearly equal to  $45^\circ$ . From (100) pole figures, it is apparent that the  $\langle 110 \rangle$  direction is at an angle of  $45^\circ$  to the  $\langle 001 \rangle$  direction. Hence if the reference plane is changed with respect to the point of origin of the grain, the direction of growth of most crystals would be close to the  $\langle 001 \rangle$  direction.

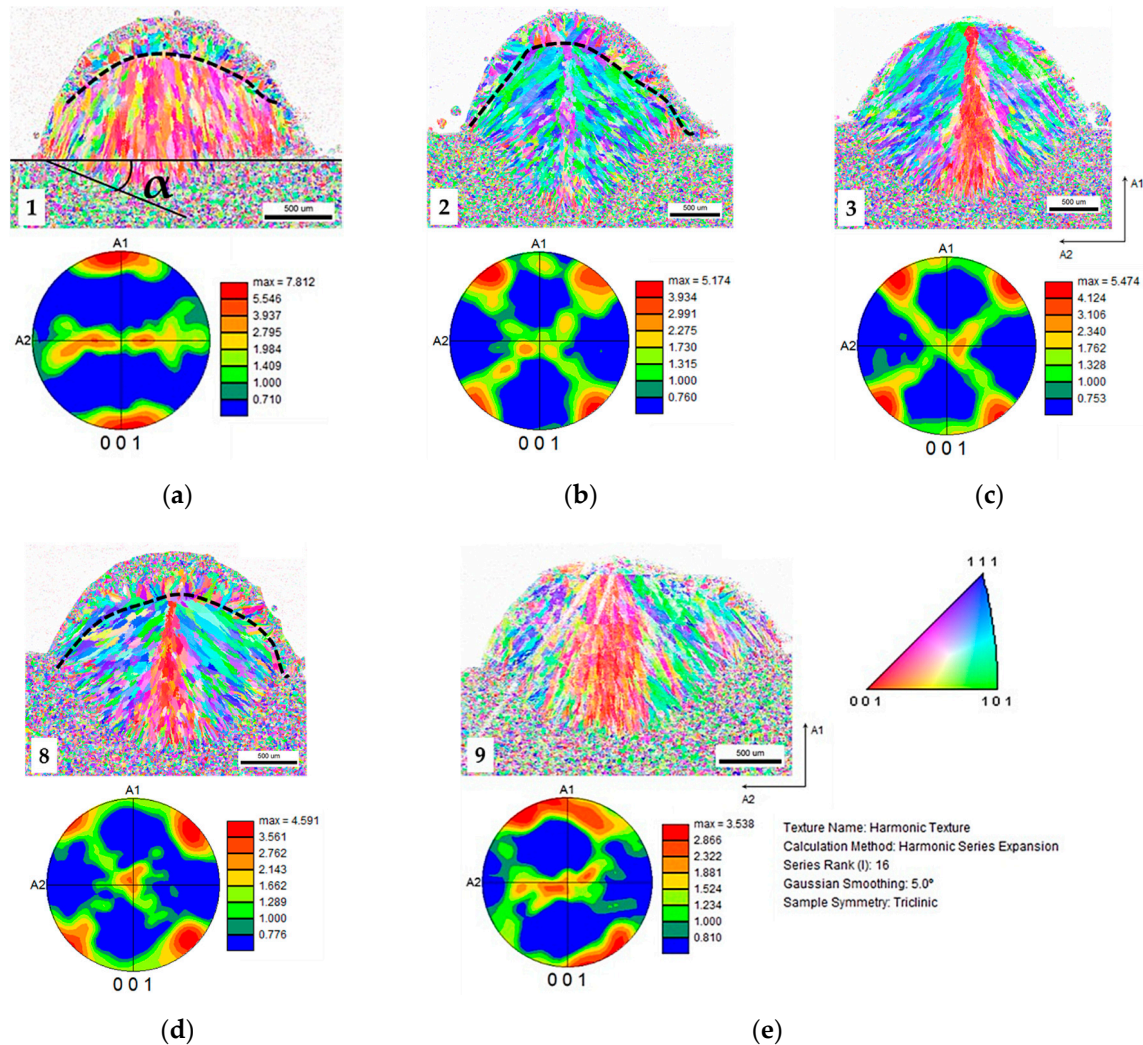


**Figure 7.** (100) IPFs (above) showing grain orientation along growth direction and respective pole figures (below) for process parameter conditions as in Table 2. The dotted line in (a,b,d) indicate columnar to equiaxed transition (CET), which is confined to a very small region in (c,e).  $\alpha$  depicts the interaction angle made by the deposit with the substrate.

The grain size measured in the middle regions for columnar grains showed a strong dependence on the laser power irrespective of scanning speeds and stand-off distances. At 1200 W corresponding to deposit 1, an average grain size of  $58 \mu\text{m}$  (ASTM 4.9) was measured. Deposit 3 processed at a laser power of 2000 W had a larger grain size of  $88 \mu\text{m}$  (ASTM 3.7). The average grain size at 1600 W was equal to  $75 \mu\text{m}$  (ASTM 4.2),  $75 \mu\text{m}$  (ASTM 4.2) and  $78 \mu\text{m}$  (ASTM 4.1) for deposit 2, 8 and 9 respectively. The grain heights and widths were measured along A1 and A2 directions as shown in Figure 7, along two different coordinate axes and along the length of the deposit. In order to incorporate most grains, the grain sizes were measured close to the deposit centerline where the power density was highest as per Gaussian form of energy distribution (as indicated in Figure 1a). Hence laser power principally influenced the power density factor of various parameter sets, thereby influencing the average grain size in the middle region of the deposit.

Much finer equiaxed grains were observed at the top part of the deposit and a bimodal grain structure existed in an intermediate layer between the columnar and equiaxed grains in deposits 1, 2 and 8. The dotted line in Figure 7a,b,d represents this change in morphology known as Columnar to Equiaxed Transition (CET) [45,46]. This is arguably due to constitutional supercooling, wherein the liquid in front of the S/L interface becomes progressively enriched with elements having low partition co-efficients (predominantly Nb in case of Alloy 718), providing the undercooling necessary for heterogeneous nucleation of grains in the solute-rich melt-pool, observed in the top region of DED deposits [44,47].

Comparison of IPFs of deposits pertaining to parameter sets 1, 8 and 3 provides an insight into the effect of varied laser power on grain structure. Notably, the diminished presence of the top region in deposits 3 and 9 was of interest as it is believed to have implications for the segregation of Nb-rich phases when subsequent layers of deposit are built on top of the existing single track specimen. The secondary growth front in these cases was hindered by the high-temperature gradients that remelted any existing dendrites and heterogeneously nucleated grains present at the top region of the deposit. The effect of varied scanning speed was negligible as deposit 2 ( $V = 900$  mm/min) and deposit 8 ( $V = 1100$  mm/min) did not show appreciable variation. Deposit 9 ( $L_o = 13$  mm) was more successful in eliminating the top region segregation, and hence the formation of equiaxed grains compared to deposit 8 ( $L_o = 9.5$  mm).

### 3.2.2. Nb-Rich Eutectic Phases

The SEM micrographs in Figure 8a–c depict the segregation patterns of Nb-rich eutectic phases represented by white particulates in the top, middle and bottom regions respectively. There are two main eutectic reactions known to occur in Alloy 718:  $1280$  °C to  $1250$  °C wherein  $\gamma$ /NbC is precipitated and the  $\gamma$ /laves phase occurring in the temperature range of  $1075$  °C to  $1200$  °C [19,41], depending on the specific alloy composition and processing conditions. Local solidification conditions at the inter-dendritic Nb rich regions formed NbCs and laves phases (Figure 8). The EDS point analyses revealed that the white particulates were indeed Nb-rich precipitates as shown in Figure 8d, for which the elemental analysis is tabulated in Table 4. Along the height of the deposit further away from the substrate, the segregation was higher and the cooling rates also decreased due to limited heat flux conditions, leading to higher inter-dendritic spacing and precipitation of more Nb-rich phases [25,28]. It is apparent from Figure 8a–c that the top regions have higher segregation of such Nb-rich eutectic phases compared to other regions, which was confirmed by the area fraction analyses as shown in Figure 8e. The modelling work performed by Nie et al. [27] provides insight into the expected cooling rates along the height of the bead and consequently the variation in secondary dendrite arm spacing for Alloy 718.

**Table 4.** Elemental analysis of point spectrum locations depicted in Figure 8d.

Element	Weight %			
	Spectrum 1	Spectrum 2	Spectrum 3	Spectrum 4
Ni	46.86	38.14	45.11	40.67
Cr	18.03	13.02	11.77	13.54
Fe	17.95	11.05	10.05	11.43
Nb	2.2	13.06	16.3	17.89
Al	0.47	0.34	0.28	0.3
Ti	0.52	1.19	1.33	1.65
Mo	2.79	3.99	-	-
C	0.22	5.3	3.73	4.68

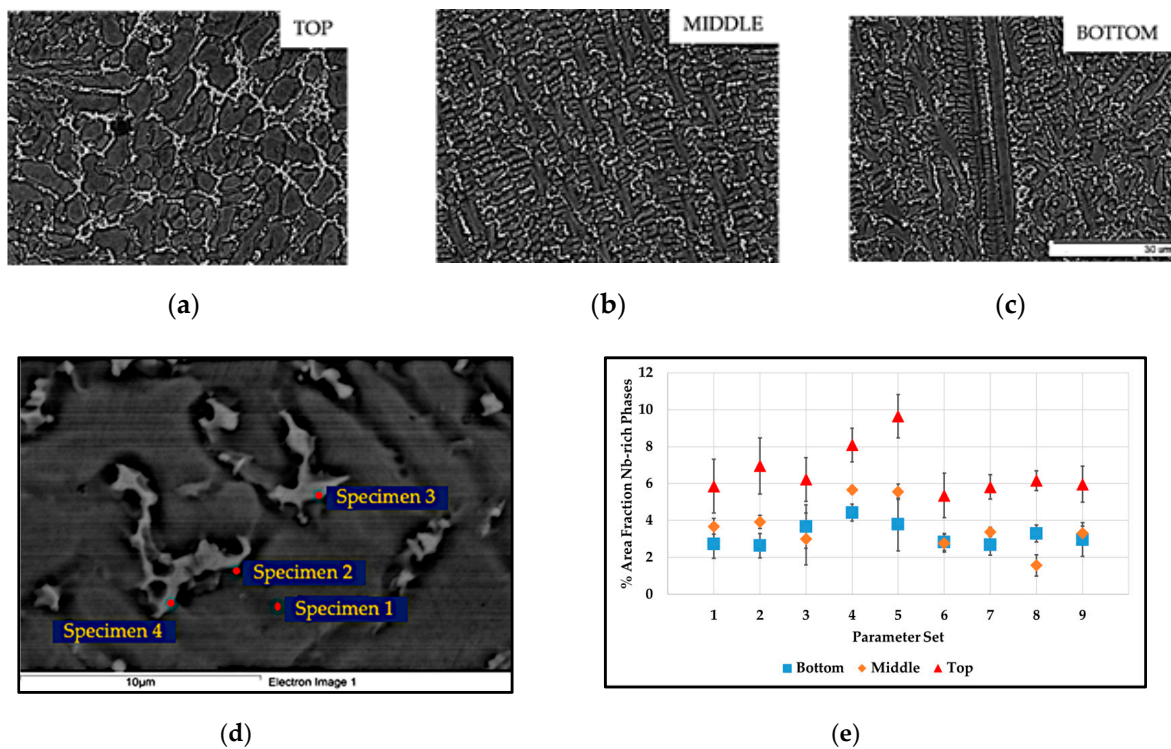


**Figure 8.** SEM Micrographs depicting variation in Nb-rich phase fraction in (a) top; (b) middle; (c) bottom regions in a deposition pertaining to parameter set 1 (refer to Table 2). (d) EDS mapping of Nb-rich precipitates (Spectrum 2–4) and matrix (Spectrum 1); (e) plot showing area fraction of Nb-rich eutectic phases for various parameters.

### 3.3. Effect of Laser Power, Scanning Speed and Laser Stand-Off Distance on Nb-Rich Phase Fraction

A qualitative conclusion can be reached by studying the effect of laser power on Nb-rich phase formation as depicted in Figure 9a–c. The Nb-rich phase fraction decreased with increased  $P$  in the case of the higher  $L_o$  of 13 mm. An opposite trend was noticed in the 9.5 mm stand-off distance condition in top and bottom regions. The segregation in the top region was primarily determined by the CET and secondary growth fronts. CET was controlled by the solute rejection and build up ahead of S/L front combined with convective currents present in the melt-pool. At higher specific energies, the thermal gradient was high enough to persist until the end of solidification of the entire deposit deterring heterogeneous nucleation of equiaxed grains. Also, the convective currents aid in better solute dissolution in the melt ahead of the growth front, thereby hindering the formation of Nb-rich phases with increasing power throughout the deposit [38,48].

The effect of scanning speeds was much clearer at a constant laser power of 1600 W. Increased scanning speed yielded fewer Nb-rich phases as in Figure 9d, with only exception of line indicating  $L_o = 9.5$  mm in the bottom region of deposit. At speeds of 900 mm/min, the conditions having a stand-off distance of 9.5 mm had higher Nb-rich area fraction compared to  $L_o$  of 13 mm. At 1100 mm/min, stand-off distances had a minimal effect on Nb-rich area fraction.

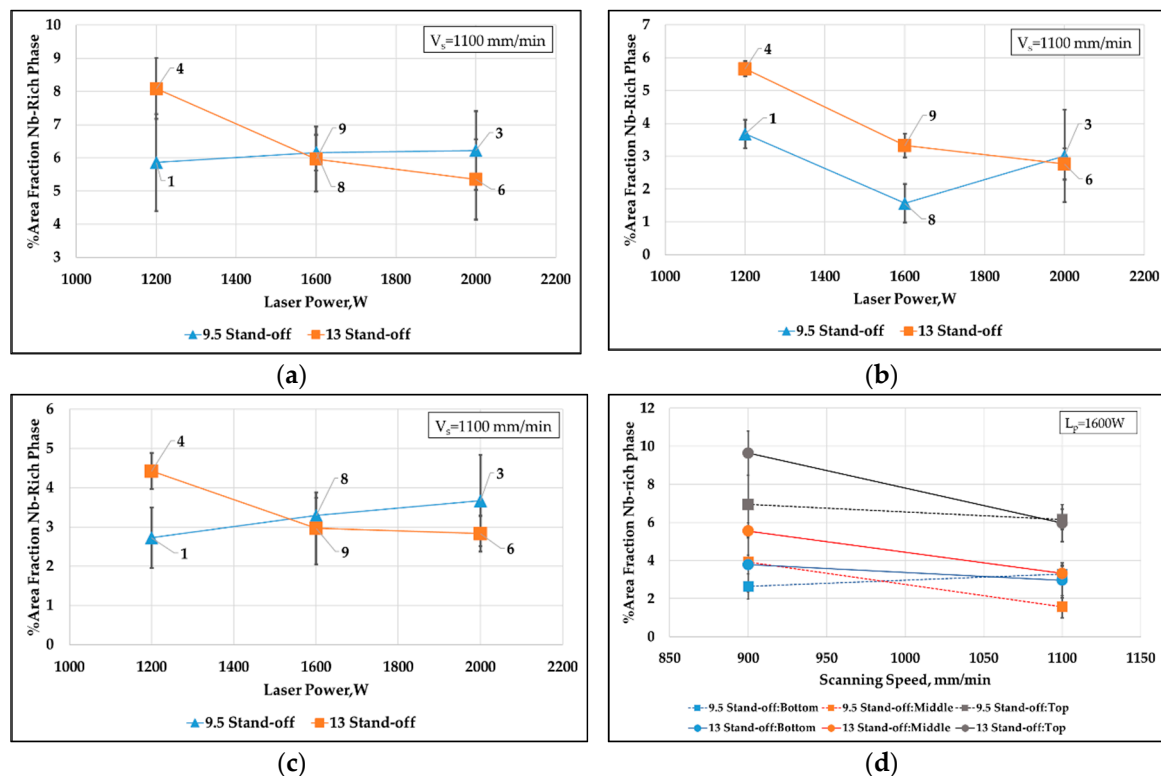


**Figure 9.** Plots depicting the effect of laser power and laser stand-off distance on (a) top region; (b) middle region; (c) bottom region. (d) Effect of scanning speed and laser stand-off distance on Nb-rich eutectic phase fractions.

#### 4. Conclusions

Laser power, scanning speed and laser stand-off distance were found to influence the geometry, microstructure and texture in DED single track specimens. The height of the deposits decreased with increased scanning speeds. Stand-off distance had no influence on height of the deposits. The width increased with increased laser power and stand-off distance but decreased with increased scanning speeds. Depth of the deposit increased with increased laser power and decreased with increase in stand-off distance. Deposits 3, 6 through 9 had aspect ratio ( $W/H$ ) of more than two. The area of dilution increased with increased specific energy. The powder capture efficiency increased with the increase in product of specific energy and spot diameter and minutely increased with increased stand-off distance. Deposits 3, 5, 6 and 7 pertaining to high power and stand-off distance (except 3) showed characteristics of effective powder utilization (more than 80%).

A single-track deposit had three distinct regions formed by varied cooling rates. Segregation of Nb-rich phases was found to be dominant in the top region of the deposit in all cases. Deposits 6–9 associated with moderate specific energy conditions proved to be effective in controlling segregation as they had Nb-rich phase fraction of less than 4% in the middle and bottom regions and under 6% in the top region. Scanning speed was found to be very influential in decreased area fraction of Nb-rich phases formed. Higher stand-off distances also showed indication of reducing the segregation.

Columnar grains dominated the deposits in all cases with a narrow region of equiaxed grains at the top. In cases of deposits that had better aspect ratio (as in deposit 3 and 9 from EBSD mapping), the equiaxed grains were confined to a minute region at the top regions of the deposit. Different morphology and orientation can be achieved by varying energy conditions. The preferred growth direction for columnar grains is  $\langle 100 \rangle$ . A center-line solidification was noticed in cases of grains that had  $\langle 110 \rangle$ ,  $\langle 111 \rangle$  orientations because of their high dilution rate, with interaction angles of nearly  $45^\circ$ . Dilution was influenced by specific energy, and hence the texture morphology was affected by power, speed and stand-off distances.

Moderate to high powers ( $P = 1800$  and  $2000$  W), high speed ( $V = 1100$  mm/min) and high stand-off distances ( $L_o = 13$  mm) corresponding to deposits 3, 6 and 7 proved to be influential in achieving good geometrical, microstructural and segregation properties. Hence, they are more suitable for building multilayered deposits as they offer better characteristics in terms of aspect ratio, dilution and powder capture efficiency. The segregation of Nb-rich phases at the top of these deposits are minimal and the equiaxed region at the top is minimal in these deposits.

**Author Contributions:** Conceptualization, methodology, investigation, writing—original draft preparation, S.S.; supervision, methodology, writing—review and editing, J.A., S.J.; EBSD investigation, E.G.; experimental work, K.H. All authors have read and agreed to the published version of the manuscript.

**Funding:** This research was funded by Vinnova, KK-SUMAN-Next and CAM2.

**Acknowledgments:** The authors acknowledge the support of GKN Aerospace AB.

**Conflicts of Interest:** The authors declare no conflict of interest.

## References

1. Domenico, A.; Angelastro, A.L.S. Experimental Analysis of the Direct Laser Metal Deposition Process. In *New Trends in Technologies: Devices, Computer, Communication and Industrial Systems*; IntechOpen: London, UK, 2010. [\[CrossRef\]](#)
2. Graf, B.; Ammer, S.; Gumenyuk, A.; Rethmeier, M. Design of Experiments for Laser Metal Deposition in Maintenance, Repair and Overhaul Applications. *Procedia CIRP* **2013**, *11*, 245–248. [\[CrossRef\]](#)
3. Boisselier, D.; Sankaré, S. Influence of Powder Characteristics in Laser Direct Metal Deposition of SS316L for Metallic Parts Manufacturing. *Phys. Procedia* **2012**, *39*, 455–463. [\[CrossRef\]](#)
4. Witzel, J.; Kelbassa, I.; Gasser, A.; Backes, G. Increasing the deposition rate of inconel 718 for LMD. In Proceedings of the International Congress on Applications of Lasers & Electro-Optics, Anaheim, CA, USA, 16–20 October 2016; pp. 304–310.
5. Abioye, T.E.; Farayibi, P.K.; Kinnel, P.; Clare, A.T. Functionally graded Ni-Ti microstructures synthesised in process by direct laser metal deposition. *Int. J. Adv. Manuf. Technol.* **2015**, *79*, 843–850. [\[CrossRef\]](#)
6. Shah, K.; Haq, I.u.; Khan, A.; Shah, S.A.; Khan, M.; Pinkerton, A.J. Parametric study of development of Inconel-steel functionally graded materials by laser direct metal deposition. *Mater. Des. (1980–2015)* **2014**, *54*, 531–538. [\[CrossRef\]](#)
7. Shah, K.; Izhar U., H.; Shah, S.A.; Khan, F.U.; Khan, M.T.; Khan, S. Experimental study of direct laser deposition of Ti-6Al-4V and Inconel 718 by using pulsed parameters. *Sci. World J.* **2014**, *2014*, 841549. [\[CrossRef\]](#) [\[PubMed\]](#)
8. Zhong, C.; Gasser, A.; Schopphoven, T.; Poprawe, R. Experimental study of porosity reduction in high deposition-rate Laser Material Deposition. *Opt. Laser Technol.* **2015**, *75*, 87–92. [\[CrossRef\]](#)
9. Sui, S.; Zhong, C.; Chen, J.; Gasser, A.; Huang, W.; Schleifenbaum, J.H. Influence of solution heat treatment on microstructure and tensile properties of Inconel 718 formed by high-deposition-rate laser metal deposition. *J. Alloys Compd.* **2018**, *740*, 389–399. [\[CrossRef\]](#)
10. Zhong, C.; Biermann, T.; Gasser, A.; Poprawe, R. Experimental study of effects of main process parameters on porosity, track geometry, deposition rate, and powder efficiency for high deposition rate laser metal deposition. *J. Laser Appl.* **2015**, *27*. [\[CrossRef\]](#)
11. Zhong, C.; Gasser, A.; Kittel, J.; Wissenbach, K.; Poprawe, R. Improvement of material performance of Inconel 718 formed by high deposition-rate laser metal deposition. *Mater. Des.* **2016**, *98*, 128–134. [\[CrossRef\]](#)
12. Zhong, C.; Gasser, A.; Kittel, J.; Fu, J.; Ding, Y.; Poprawe, R. Microstructures and tensile properties of Inconel 718 formed by high deposition-rate laser metal deposition. *J. Laser Appl.* **2016**, *28*. [\[CrossRef\]](#)
13. Elefterie, C.F.; Guragata, C.; Bran, D.; Ghiban, B. Aeronautical requirements for Inconel 718 alloy. *IOP Conf. Ser. Mater. Sci. Eng.* **2017**, *209*. [\[CrossRef\]](#)
14. Radavich, J.F. Superalloy 718—A Look at the First 30 Years. *JOM* **2012**, *40*, 35. [\[CrossRef\]](#)
15. Loria, E.A. The Status and Prospects of Alloy 718. *JOM* **2012**, *40*, 36–41. [\[CrossRef\]](#)
16. Radhakrishna, C.; Rao, K.P.; Srinivas, S. Laves phase in superalloy 718 weld metals. *J. Mater. Sci. Lett.* **1995**, *14*, 1810–1812. [\[CrossRef\]](#)

17. Cieslak, M.J.; Knorovsky, G.A.; Headley, T.J.; Romig, J.A.D. The Solidification Metallurgy of Alloy 718 and Other Nb-Containing Superalloys. In Proceedings of the Superalloys 718 Metallurgy and Applications (1989), Pittsburgh, PA, USA, 12–14 June 1989; pp. 59–68.
18. Ogborn, J.S.; Olson, D.L.; Cieslak, M.J. Influence of solidification on the microstructural evolution of nickel base weld metal. *Mater. Sci. Eng. A* **1995**, *203*, 134–139. [[CrossRef](#)]
19. Knorovsky, G.A.; Cieslak, M.J.; Headley, T.J.; Romig, A.D.; Hammett, W.F. INCONEL 718: A solidification diagram. *Metall. Trans. A* **1989**, *20*, 2149–2158. [[CrossRef](#)]
20. Janaki Ram, G.D.; Venugopal Reddy, A.; Prasad Rao, K.; Madhusudhan Reddy, G. Control of Laves phase in Inconel 718 GTA welds with current pulsing. *Sci. Technol. Weld. Join.* **2013**, *9*, 390–398. [[CrossRef](#)]
21. Manikandan, S.G.K.; Sivakumar, D.; Rao, K.P.; Kamaraj, M. Effect of weld cooling rate on Laves phase formation in Inconel 718 fusion zone. *J. Mater. Process. Technol.* **2014**, *214*, 358–364. [[CrossRef](#)]
22. Manikandan, S.G.K.; Sivakumar, D.; Rao, K.P.; Kamaraj, M. Effect of enhanced cooling on microstructure evolution of alloy 718 using the gas tungsten arc welding process. *Weld. World* **2016**, *60*, 899–914. [[CrossRef](#)]
23. Xiao, H.; Li, S.; Han, X.; Mazumder, J.; Song, L. Laves phase control of Inconel 718 alloy using quasi-continuous-wave laser additive manufacturing. *Mater. Des.* **2017**, *122*, 330–339. [[CrossRef](#)]
24. Xiao, H.; Li, S.M.; Xiao, W.J.; Li, Y.Q.; Cha, L.M.; Mazumder, J.; Song, L.J. Effects of laser modes on Nb segregation and Laves phase formation during laser additive manufacturing of nickel-based superalloy. *Mater. Lett.* **2017**, *188*, 260–262. [[CrossRef](#)]
25. Chen, Y.; Guo, Y.; Xu, M.; Ma, C.; Zhang, Q.; Wang, L.; Yao, J.; Li, Z. Study on the element segregation and Laves phase formation in the laser metal deposited IN718 superalloy by flat top laser and gaussian distribution laser. *Mater. Sci. Eng. A* **2019**, *754*, 339–347. [[CrossRef](#)]
26. Amine, T.; Newkirk, J.W.; Liou, F. Investigation of effect of process parameters on multilayer builds by direct metal deposition. *Appl. Therm. Eng.* **2014**, *73*, 500–511. [[CrossRef](#)]
27. Nie, P.; Ojo, O.A.; Li, Z. Modeling analysis of laser cladding of a nickel-based superalloy. *Surf. Coat. Technol.* **2014**, *258*, 1048–1059. [[CrossRef](#)]
28. Nie, P.; Ojo, O.A.; Li, Z. Numerical modeling of microstructure evolution during laser additive manufacturing of a nickel-based superalloy. *Acta Mater.* **2014**, *77*, 85–95. [[CrossRef](#)]
29. Parimi, L.L.; Ravi, A.G.; Clark, D.; Attallah, M.M. Microstructural and texture development in direct laser fabricated IN718. *Mater. Charact.* **2014**, *89*, 102–111. [[CrossRef](#)]
30. Dinda, G.P.; Dasgupta, A.K.; Mazumder, J. Texture control during laser deposition of nickel-based superalloy. *Scr. Mater.* **2012**, *67*, 503–506. [[CrossRef](#)]
31. Chen, B.; Mazumder, J. Role of process parameters during additive manufacturing by direct metal deposition of Inconel 718. *Rapid Prototyp. J.* **2017**, *23*, 919–929. [[CrossRef](#)]
32. Segerstark, A.; Andersson, J.; Svensson, L.-E. Investigation of laser metal deposited Alloy 718 onto an EN 1.4401 stainless steel substrate. *Opt. Laser Technol.* **2017**, *97*, 144–153. [[CrossRef](#)]
33. ASTM. F3055-14a, *Standard Specification for Additive Manufacturing Nickel Alloy (UNS N07718) with Powder Bed Fusion*; ASTM International: West Conshohocken, PA, USA, 2014. [[CrossRef](#)]
34. ASTM. B670-07, *Standard Specification for Precipitation-Hardening Nickel Alloy (UNS N07718) Plate, Sheet, and Strip for High-Temperature Service*; ASTM International: West Conshohocken, PA, USA, 2018. [[CrossRef](#)]
35. International, A. ASTM E112-13, *Standard Test Methods for Determining Average Grain Size*; ASTM: West Conshohocken, PA, USA, 2013. [[CrossRef](#)]
36. de Oliveira, U.; Ocelík, V.; De Hosson, J.T.M. Analysis of coaxial laser cladding processing conditions. *Surf. Coat. Technol.* **2005**, *197*, 127–136. [[CrossRef](#)]
37. Corbin, D.J.; Nassar, A.R.; Reutzel, E.W.; Beese, A.M.; Kistler, N.A. Effect of directed energy deposition processing parameters on laser deposited Inconel®718: External morphology. *J. Laser Appl.* **2017**, *29*. [[CrossRef](#)]
38. DuPont, J.N. Fundamentals of Weld Solidification. In *Welding Fundamentals and Processes*; Lienert, T.S.T., Babu, S., Acoff, V., Eds.; ASM International: West Conshohocken, PA, USA, 2011; pp. 96–114. [[CrossRef](#)]
39. Trivedi, R.; David, S.A.; Eshelman, M.A.; Vitek, J.M.; Babu, S.S.; Hong, T.; DebRoy, T. In situ observations of weld pool solidification using transparent metal-analog systems. *J. Appl. Phys.* **2003**, *93*, 4885–4895. [[CrossRef](#)]
40. David, S.A.; Babu, S.S.; Vitek, J.M. Welding: Solidification and microstructure. *JOM* **2003**, *55*, 14–20. [[CrossRef](#)]
41. Antonsson, T.; Fredriksson, H. The effect of cooling rate on the solidification of INCONEL 718. *Metall. Mater. Trans. B* **2005**, *36*, 85–96. [[CrossRef](#)]

42. Patel, A.D.; Murty, Y.V. Effect of Cooling Rate on Microstructural Development in Alloy 718. In *Superalloys 718, 625, 706 and Various Derivatives*; Carpenter Technology Corporation: Pittsburgh, PA, USA, 2001; pp. 124–132.
43. Dong, H.B.; Yang, X.L.; Lee, P.D.; Wang, W. Simulation of equiaxed growth ahead of an advancing columnar front in directionally solidified Ni-based superalloys. *J. Mater. Sci.* **2004**, *39*, 7207–7212. [[CrossRef](#)]
44. Gäumann, M.; Henry, S.; Cléton, F.; Wagnière, J.D.; Kurz, W. Epitaxial laser metal forming: Analysis of microstructure formation. *Mater. Sci. Eng. A* **1999**, *271*, 232–241. [[CrossRef](#)]
45. Hunt, J.D. Steady state columnar and equiaxed growth of dendrites and eutectic. *Mater. Sci. Eng.* **1984**, *65*, 75–83. [[CrossRef](#)]
46. Kurz, W.; Bezençon, C.; Gäumann, M. Columnar to equiaxed transition in solidification processing. *Sci. Technol. Adv. Mater.* **2001**, *2*, 185–191. [[CrossRef](#)]
47. Gäumann, M.; Bezençon, C.; Canalis, P.; Kurz, W. Single-crystal laser deposition of superalloys: Processing–microstructure maps. *Acta Mater.* **2001**, *49*, 1051–1062. [[CrossRef](#)]
48. Porter, A.D.; Easterling, K.E.; Sherif, M.Y. *Phase Transformations in Metals and Alloys*, 3rd ed.; CRC Press: Boca Raton, FL, USA, 2009; p. 536. [[CrossRef](#)]



© 2020 by the authors. Licensee MDPI, Basel, Switzerland. This article is an open access article distributed under the terms and conditions of the Creative Commons Attribution (CC BY) license (<http://creativecommons.org/licenses/by/4.0/>).